TRANSNAV
http://www.transnav.eu
the International Journal
on Marine Navigation
and Safety of Sea Transportation
Volume 19
Number 2
June 2025
DOI: 10.12716/1001.19.02.04

A Novel Network RTK Technique for Mobile Platforms: Extending High-Precision Positioning to Offshore Environments

W. Chen, J. Ding, Y. Wang, X. Mi & T. Liu
The Hong Kong Polytechnic University, Hong Kong

ABSTRACT: Network Real-Time Kinematic (NRTK) positioning, as the most mature real-time high-precision positioning technology, is widely recognized for its centimetre-level accuracy, operational efficiency, and extensive application potential. However, conventional NRTK systems rely on reference stations anchored to bedrock-based infrastructure, limiting their coverage to terrestrial areas within Continuous Operating Reference Station (CORS) networks. This architectural limitation renders conventional NRTK inapplicable for offshore and marine environments. To overcome this geographical constraint, we propose an innovative NRTK framework for mobile platforms featuring (1) simultaneous estimation of atmospheric delays and baseline dynamics to get precise relative coordinate movements, (2) the regularization method is applied to de-correlate the positional and atmospheric parameters and the regularization coefficients are optimized by mean square error minimization, and (3) integration of Precise Point Positioning (PPP) at a main base station to maintain an absolute position reference for the network. Experimental validation using Hong Kong's terrestrial CORS network demonstrates that the proposed marine-adapted system achieves positioning accuracy comparable to conventional bedrock-based NRTK, with three-dimensional (ENU) errors measuring (2.90, 3.22, 4.32) cm and (2.90, 2.88, 6.70) cm in two operational scenarios. This methodological advancement enables the deployment of buoy-based NRTK systems in marine environments, with significant implications for maritime applications including port traffic management, fishing fleet navigation, and offshore resource exploration. By extending NRTK's operational domain beyond terrestrial boundaries, our technique not only enhances positioning reliability for marine operations but also creates new paradigms for oceanic resource management.

1 INTRODUCTION

With the development of advanced Global Navigation Satellite System (GNSS) infrastructures, hardware, and data processing strategies, real-time high precision positioning with centimetre level accuracy has been widely available to support diversified applications, such as surveying and mapping [1], precise agriculture [2], seismology [3], autonomous vehicle [4], atmospheric sensing [5], and scientific research [6], [7]. Conventional Real-Time Kinematic (RTK) technologies require a geodetic infrastructure with a regional reference station network and low-cost communication link (i.e. mobile communication network) in the coverage region [8], [9]. This will not available for offshore applications. Currently, for offshore high precision positioning applications, there are mainly two technologies, including Wide Area Differential GNSS (WADGNSS, i.e. US WAAS, European EGNOS systems) and Precise Point Positioning (PPP) Systems (i.e., BeiDou, Galileo, Trimble RTX) from different governmental or industrial organizations [10]–[14]. WADGNSS systems is originally designed to satisfy high reliability navigation services for civil aviation

which can achieve meter level positioning accuracy with high integrity [15]. Kinematic PPP technology utilizes the high-quality orbit and satellite clock error products from a global network (i.e. International GNSS Services (IGS)) to provide decimetre level positioning worldwide with a single user receiver [16], [17]. However, with the PPP approach the vertical positioning accuracy is relatively lower (decimetre level) and the convergence time is relatively long (typical 30 min), compared with conventional land based RTK technology with the ambiguity fixing time of a few seconds [18]–[20]. These restrict some applications requiring higher accuracy (centimetre level) and quick setup in offshore applications [21]–[25]. Another possible way is the moving-base positioning mode, while it is not designed for ocean positioning, and existing studies on mobile base stations focus on moving base positioning models, which mainly focus on ambiguity fixation of a single ultra-short moving baseline, with application scenarios of two moving cars [26]–[28], or unmanned aerial vehicles (UAVs) [29], [30]. These scenarios usually do not estimate atmospheric parameters and do not provide external positioning services like NRTK. Therefore, they cannot provide solutions and effective decorrelation methods need to be introduced to improve the accuracy of the solutions.

A promising way to extend GNSS technology to the offshore area is to equip floating objects at sea with GNSS receivers, such as shipboard GNSS [31]–[33] and buoy-based GNSS [34], [35]. The former usually only stays in a certain area for a short time and has only a single receiver, or multiple receivers on a single ship, and cannot provide stable positioning services to the area. The latter is more costly as the buoy needs to be cemented to the anchor chain to prevent loss of the buoy due to the action of ocean currents. Existing marine GNSS studies have focused on reconstructing seafloor horizontal displacement [36], acoustic seafloor positioning precision [37], [38], testing the effectiveness of short message communication [39], significant wave height retrieval [40], [41], sea surface salinity retrieval [42], meteorological tsunami monitoring [43], and water level measurements [44]. These studies typically give little consideration to communication between multiple offshore GNSS receivers and have never considered the construction of an offshore GNSS network to provide continuous positioning service to the region. In addition, the high coupling qualities of vertical position movement estimates with tropospheric delays in a dynamic setting have not been extensively studied.

In this study, we aim to develop a new GNSS positioning method which extends high-precision NRTK positioning for mobile platforms for offshore industry, where conventional network RTK is not covered. This method effectively combines the advantages of PPP and RTK. By utilizing the services provided through this method, users can achieve precise absolute positioning comparable to PPP, while retaining the rapid convergence advantage characteristic of NRTK. All GNSS users around the kinematic reference stations in offshore environment will be able to achieve real-time, and centimetre level positioning accuracy, similar to the performance of conventional land-based NRTK operation. Table 1 shows the comparison of several existing methods of offshore positioning, including PPP, traditional NRTK, moving-base positioning solution and the method this research proposed.

Table 1. Comparison of several methods of offshore positioning

Solutions	High accuracy	Fast convergence	With regularization	Offshore
PPP	✓	×	×	✓
NRTK	✓	✓	×	×
Moving-base	✓ (relative)	✓	×	✓
This research	✓	✓	✓	✓

We introduce the traditional NRTK method for fixed base stations in Section 2, followed by its adaptation for mobile base stations. Then the regularization technique to decorrelate unknown parameters and detail the computation of the regularization parameter is described. Section 3 compares parameter estimation of baseline solutions between fixed and mobile base station NRTK methods using the Hong Kong CORS network data, evaluates the impact of regularization, and presents positioning validation results. Finally, we give conclusions and outlooks in Section 4.

2 METHODS

In this section, we first introduce the traditional NRTK for fixed-base station platforms, then describe how it can be extended to NRTK for mobile platforms, next describe the introduction of regularization methods to de-correlate between the parameters to be estimated, and finally introduce the method for determining the regularization parameters.

2.1 *RTK for fixed base stations*

Observation equations of GNSS code pseudorange (P) and carrier phase (Φ) measurements from a satellite s to a receiver r with frequency f can be expressed as:

$$\begin{aligned} P_{r,f}^s &= \rho_r^s + t_r - t^s + T_r^s + I_{r,f}^s + b_{P_{f,r}} - b^{P_{f,s}^s} + M_{r,f}^s + \delta_{r,rel}^s + \varepsilon_{P_{r,f}^s} \\ \Phi_{r,f}^s &= \rho_r^s + t_r - t^s + T_r^s - I_{r,f}^s + b_{\Phi_{f,r}} - b^{\Phi_{f,s}^s} + \lambda_f N_{r,f}^s + M_{r,f}^s + \delta_{r,rel}^s + \varepsilon_{\Phi_{r,f}^s} \end{aligned} \tag{1}$$

in which ρ_r^s is the geometric distance between the phase centres of satellite and receiver antennas. t_r and t^s are the receiver clock and satellite clock respectively. T_r^s and $I_{r,f}^s$ are tropospheric delay and ionospheric delay respectively. b is the device delay and M is the multipath delay. δ and ε are relativistic effects and observational noise. N are the phase ambiguities, λ is the wavelength of signal with frequency f.

By combining the observation equations of frequency f_1 and f_2, we can get the double difference (DD) observation equation:

$$\begin{aligned} \nabla\Delta P_{f_1} &= \nabla\Delta\rho + \nabla\Delta I_{f_1} + \nabla\Delta T + \nabla\Delta\varepsilon_{P_{f_1}} \\ \nabla\Delta P_{f_2} &= \nabla\Delta\rho + \nabla\Delta I_{f_2} + \nabla\Delta T + \nabla\Delta\varepsilon_{P_{f2}} \\ \nabla\Delta\Phi_{f_1} &= \nabla\Delta\rho - \nabla\Delta I_{f_1} + \nabla\Delta T + \lambda_{f_1}\nabla\Delta N_{f_1} + \nabla\Delta\varepsilon_{\Phi_{f_1}} \\ \nabla\Delta\Phi_{f_2} &= \nabla\Delta\rho - \nabla\Delta I_{f_2} + \nabla\Delta T + \lambda_{f_2}\nabla\Delta N_{f_2} + \nabla\Delta\varepsilon_{\Phi_{f_2}} \end{aligned} \tag{2}$$

where $\nabla\Delta$ is the double difference sign and the rest are the same as before. By using the double-difference method, the majority of common errors in conventional RTK positioning are eliminated.

Then, the Melbourne–Wubbena (MW) combination is used to determine wide-lane (WL) integer ambiguities:

$$\nabla\Delta\Phi_{MW} = \nabla\Delta\Phi_{WL} - \nabla\Delta P_{NL} = \nabla\Delta N_{WL}\cdot\lambda_{WL} + \nabla\Delta\varepsilon_{P_{NL}} \tag{3}$$

$$\nabla\Delta\Phi_{WL} = \frac{f_1\nabla\Delta P_{f_1} - f_2\nabla\Delta P_{f_2}}{f_1 - f_2} \tag{4}$$

$$\nabla\Delta P_{NL} = \frac{f_1\nabla\Delta P_{f_1} + f_2\nabla\Delta P_{f_2}}{f_1 + f_2} \tag{5}$$

$$\nabla\Delta N_{WL} = \nabla\Delta N_{f_1} - \nabla\Delta N_{f_2} \tag{6}$$

$$\lambda_{WL} = \frac{c}{f_1 - f_2} \tag{7}$$

After that, the ionosphere-free combination (IF) approach is used to estimate the L1 ambiguity [45]. The only remaining unknown parameters to calculate are the geometric distance and the tropospheric delay.

$$\begin{aligned}\nabla\Delta\Phi_{IF} &= \frac{\gamma\cdot\nabla\Delta\Phi_1 - \nabla\Delta\Phi_2}{\gamma - 1} - \frac{1}{2}\left(\lambda_{WL} + \lambda_{NL}\right)\cdot\nabla\Delta N_{WL} \\ &= \nabla\rho + \nabla\Delta\delta R + \nabla\Delta T + \nabla\Delta N_{f_2}\lambda_{NL} + \nabla\Delta\varepsilon_{\Phi_{IF}}\end{aligned} \tag{8}$$

$$\gamma = \frac{(f_1)^2}{(f_2)^2} \tag{9}$$

For the traditional NRTK, the DD geometric distance is solved by using the known fixed base station coordinates. Then the relative tropospheric delay remaining as an unknown parameter matrix **X**:

$$\mathbf{x} = [\Delta T] \tag{10}$$

Then, the tropospheric delay is estimated by the following least squares (LS) method:

$$\begin{aligned}\mathbf{N}_x &= \mathbf{A}^T\mathbf{P}\mathbf{A} \\ \mathbf{W}_x &= \mathbf{A}^T\mathbf{P}\mathbf{l} \\ \mathbf{X}_x &= \mathbf{N}_x^{-1}\mathbf{W}_x\end{aligned} \tag{11}$$

where **A** is the coefficient matrix, **P** is the weight matrix and **I** is their noise vectors.

2.2 *RTK for mobile base stations*

As for the mobile platform, all base stations are located at sea and are in constant motion, making their exact coordinates unknown. Consequently, the relative movement of the base stations' coordinates is also incorporated into the matrix of unknown parameters. Figure 1 shows a minimal triangulation NRTK diagram from a fixed platform to a mobile platform.

$$\mathbf{x} = [\Delta x, \Delta y, \Delta z, \Delta T] \tag{12}$$

At this point, the number of observations is still greater than the number of unknown parameters, so the equation is solved. But the change in the number of unknown parameters obviously weakens the strength of the equation. In addition, due to the poor geometric configuration of the satellite in the vertical direction, the unknown parameters in the U-direction are usually strongly coupled with the tropospheric parameters, and this coupling will lead to a decrease in the accuracy of the solution when the base stations are all in a constant state of movement.

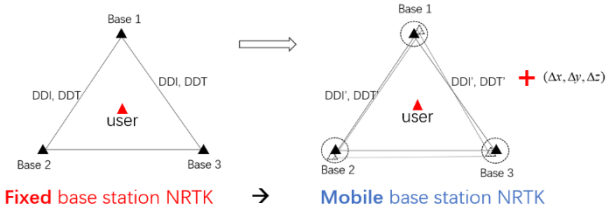

Figure 1. Schematic diagram of fixed base station NRTK to mobile base station NRTK

2.3 *RTK for mobile base stations with regularized solution*

We introduce the following regularization methods to de-correlate the parameters and thus improve the accuracy of the solution.

$$\mathbf{N}_\alpha = \mathbf{A}^T\mathbf{P}\mathbf{A} + \mathbf{S} \tag{13}$$

$$\mathbf{X}_\alpha = \mathbf{N}_\alpha^{-1}\mathbf{W}_x \tag{14}$$

where α is the regularization parameter and **S** is the regularization matrix. They are defined as [46]:

$$\mathbf{S} = \begin{bmatrix}\alpha\mathbf{I}_3 & 0 \\ 0 & 0\end{bmatrix} \tag{15}$$

where $\mathbf{I}_3$ is 3x3 identity matrix , the LS method calculates the unknown estimate under the regularization criterion as:

$$(\mathbf{A}\mathbf{x} - \mathbf{y})^T\mathbf{Q}^{-1}(\mathbf{A}\mathbf{x} - \mathbf{y}) + \alpha\mathbf{x}^T\mathbf{x} = \min \tag{16}$$

The solution for the estimate is:

$$\begin{aligned}\mathbf{x}_R &= \left(\mathbf{A}^T\mathbf{Q}^{-1}\mathbf{A} + \alpha\mathbf{I}_m\right)^{-1} \\ \mathbf{A}^T\mathbf{Q}^{-1}\mathbf{y} &= \mathbf{N}_\alpha^{-1}\mathbf{A}^T\mathbf{Q}^{-1}\mathbf{y} \\ \mathbf{\Sigma}_{\mathbf{x}_R} &= \sigma_0^2\mathbf{N}_\alpha^{-1}\mathbf{N}_\mathbf{x}\mathbf{N}_\alpha^{-1}\end{aligned} \tag{17}$$

The accuracy of the regularization solution is usually evaluated by the mean square error taking into account the influence of the deviation.

$$\mathbf{M}_{\mathbf{x}_R} = \mathbf{\Sigma}_{\mathbf{x}_R} + \mathbf{g}_{\mathbf{x}_R}\mathbf{g}_{\mathbf{x}_R}^T = \mathbf{N}_\alpha^{-1}\left(\sigma_0^2\mathbf{N}_\mathbf{x} + \alpha^2\bar{\mathbf{x}}^T\right)\mathbf{N}_\alpha^{-1} \tag{18}$$

2.4 *Determination of regularization parameter*

Choosing the regularization parameter demands a fine balance to ensure that the solution is both efficient and accurate. Setting it too high can overshadow the importance of observations, increasing deviation, while setting it too low might not effectively reduce noise. Techniques such as the discrepancy principle [47], the general discrepancy principle (GDP) method [47], the generalized cross-validation (GCV) [48] and the L-curve method [49], [50] are all used to determine this parameter. The L-curve method is popular but can lead to over-regularization if not carefully applied [51]. It is important to recognize that each method has its unique strengths and weaknesses, and they are best suited to specific scenarios. There is no one-size-fits-all criterion that is universally superior across all applications. In this study, we adopted the method of [52], which is valid for this study and the description is given in the following.

To ensure the validity of the parameter estimates, the mean square error is minimized to compute the regularization parameter:

$$\alpha = \arg\min_{\alpha>0} \operatorname{tr}\left(\mathbf{M}_{\mathbf{x}_R}\right) \tag{19}$$

For $\forall \alpha > 0$, $\partial^2 tr(\mathbf{M}_{\mathbf{x}_R}) / \partial \alpha^2$ holds, i.e. there exists a unique extreme point of the function. Therefore, the simplest method is to give a reasonable search interval and step size for $\alpha > 0$. According to [53], the spectral decomposition equation of the mean-variance matrix trace can be obtained:

$$\operatorname{tr}\left(\mathbf{M}_{\hat{\mathbf{x}}_R}\right) = \sigma_0^2 \sum_{i=1}^{n} \frac{\theta_i}{\left(\theta_i + \alpha\right)^2} + \alpha^2 \sum_{i=1}^{n} \frac{\left(\mathbf{v}_i \bar{\mathbf{x}}\right)^2}{\left(\theta_i + \alpha\right)^2} \tag{20}$$

where v_i is the i-th column vector of $\mathbf{V}$. Solve the following equations:

$$\partial \operatorname{tr}\left(\mathbf{M}_{\mathbf{x}_R}\right) / \partial \alpha = \sum_{i=1}^{n} \theta_i \left(\left(\mathbf{v}_i \bar{\bar{\mathbf{x}}}\right)^2 \alpha - \sigma_0^2 \right) / \left(\theta_i + \alpha\right)^3 = 0 \tag{21}$$

The optimal valuation of α is obtained. The equations can be solved using the theorem based on the median of continuous functions on a closed interval.

However, the determination of the regularization parameter requires the true value of the parameter, but the true value of the parameter is unknown, which constitutes the difficulty of the regularization method. Commonly, the LS estimation is employed instead of the true value, that is:

$$\bar{\bar{\mathbf{x}}}\bar{\bar{\mathbf{x}}}^T \mapsto \mathbf{x}_L \mathbf{x}_L^T = \mathbf{N}_{\mathbf{x}}^{-1} \mathbf{A}^T \mathbf{Q}^{-1} \mathbf{y} \mathbf{y}^T \mathbf{Q}^{-1} \mathbf{A} \mathbf{N}_{\mathbf{x}}^{-1} \tag{22}$$

However, if the un-iterated LS valuation is employed, the regularization parameter α becomes too small because its value is prone to be large, which makes it challenging to achieve a regularization effect. If the iterated LS estimation is utilized, then:

$$\mathbf{v}\mathbf{v}^T \approx E\left(\mathbf{v}\mathbf{v}^T\right) = E\left(\mathbf{e}\mathbf{e}^T\right) = \sigma_0^2 \mathbf{Q} \tag{23}$$

$$\bar{\bar{\mathbf{x}}}\bar{\bar{\mathbf{x}}}^T \mapsto \mathbf{x}_L \mathbf{x}_L^T \approx \sigma_0^2 \mathbf{N}_{\mathbf{x}}^{-1} \mathbf{A}^T \mathbf{Q}^{-1} \mathbf{Q} \mathbf{Q}^{-1} \mathbf{A} \mathbf{N}_{\mathbf{x}}^{-1} = \sigma_0^2 \mathbf{N}_{\mathbf{x}}^{-1} = \sigma_0^2 \mathbf{Q}_{\mathbf{x}_L} \tag{24}$$

In the ill-posed model, the covariance matrix $\mathbf{Q}_{\mathbf{x}_L}$ of the parameter LS valuation remains unstable. Therefore, other methods or observations can be used to calculate the initial value of the parameter $\mathbf{x}$ and its covariance matrix $\mathbf{Q}_{\mathbf{x}}$, i.e.:

$$\bar{\bar{\mathbf{x}}}\bar{\bar{\mathbf{x}}}^T \mapsto \mathbf{\Sigma}_{\mathbf{x}} = \sigma_0^2 \mathbf{Q}_{\mathbf{x}} \tag{25}$$

Then the regularization parameter can be gotten:

$$\alpha = \arg\min tr(\mathbf{N}_{\alpha}^{-1}(\mathbf{N}_{\mathbf{X}} + \alpha^2 \mathbf{Q}_x)\mathbf{N}_{\alpha}^{-1}) \tag{26}$$

Given that the geometry of the satellites is roughly uniformly distributed horizontally, the higher coupling is primarily attributed to coordinate error in the vertical direction and tropospheric delay, we propose the following changes to the regularization parameter and regularization matrix:

$$\mathbf{S} = \operatorname{diag}\left(\begin{bmatrix}\alpha_h & \alpha_h & \alpha_v\end{bmatrix} R_m, 0\right) \tag{27}$$

where R_m is the rotation matrix from local East, North, Up (ENU) coordinates to the Earth Centred Earth Fixed (ECEF) coordinates, and α_h and α_v are the regularization parameters in the horizontal and vertical directions, respectively.

3 EXPERIMENT RESULTS AND DISCUSSIONS

In this section, we will first present the experimental design, which encompasses experimental data and data processing methods. Subsequently, we compare the results obtained under two settings: one where the relative motion of the baseline is estimated and the other where it is not estimated (i.e. traditional method). Then, we compare the results of baseline solution achieved by using regularization method with those obtained without using regularization method. Finally, comparisons of user positioning results in different scenarios are given.

3.1 *Experimental setup*

The experimental data comes from a total of 8 hours from 16:00 to 24:00 on 25 March 2024 at 15 Hong Kong SatRef stations. The results of the HKST-HKPC baseline are used to show. The baseline length of HKST-HKPC is 19.4 km (see Fig. 2). The acquisition rate of the selected data is 1 second. Figure 3 shows the distribution of the 15 Hong Kong CORS GNSS stations used in the experiment, and the baseline network formed by these GNSS stations. The length of these baselines ranges from a few kilometres to more than two dozen kilometres. The correction models and estimation strategies for NRTK of server side and user side are show in Table 2. It should be noted that Fig. 3 shows the baseline distribution at the epoch when all the stations are able to receive data normally. There are some epochs where data from some stations are interrupted, at these epochs the triangulation network is reconfigured, and the full baselines can be seen in Table 3.

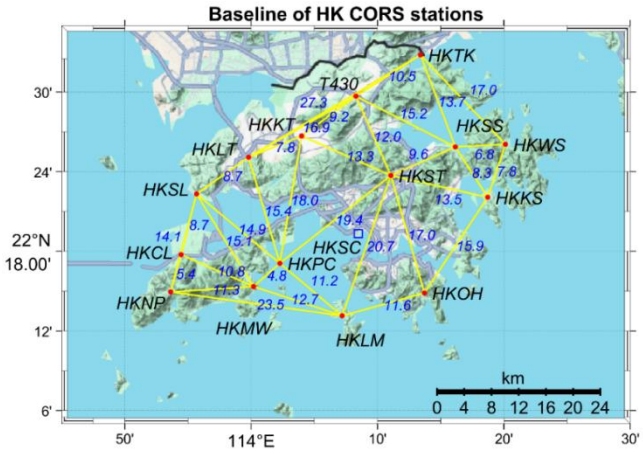

Figure 2. The test stations (red dots) selected for the experiment and corresponding baselines (yellow lines). The blue numbers represent the baseline length in kilometres. The blue square symbol corresponds to the user station HKSC used for positioning verification and does not participate in NRTK network construction.

Table 2. Correction models and estimation strategies for NRTK positioning

Items	Server side	User side
GNSS systems	GPS, Galileo, BeiDou	GPS, Galileo, BeiDou
Data sampling	1 s	30 s
A priori noise	Pseudorange: 0.3 m; carrier-phase: 0.003 m	
GNSS orbit and clock	Broadcast ephemeris	
Combination mode	Ionosphere-free combination	Double difference L1&L2
Elevation mask	20°	20°
Estimator	Sequential least squares	Extended Kalman filter
Weight of observation	Elevation-dependent weight	
Phase ambiguties	WL-L1 cascade fixing with Constants for each continuous observation arc	L1&L2 partial fixing with Constants for each continuous observation arc
Receiver coordinate	Fixed, Mobile	Kinematic
Ionospheric delays	First order eliminates, higher order ignore	Corrected by linear interpolation model (LIM)
Tropospheric delays	Hydrostatic component: modeled by Sasstamoinen with Neil mapping function (NMF); Wet component: hourly constants with process noise of 1 cm √h and NMF	Corrected by linear interpolation model (LIM)

3.2 *Comparison of estimating and not estimating the relative coordinates*

Figure 3 shows the results of the baseline HKST-HKPC. The upper panels show the time series of tropospheric delay (ΔZWD) and double-difference atmosphere (DDI and DDT) without estimating the relative movement of the base stations. The lower panels of the figures show the time series of the above three parameters as well as the three additional coordinates (Δe, Δn, Δu) when estimating the relative movement of the base stations. Where e, n, and u are the north, east, and up directions, respectively.

From the figures, we can see that, after estimating three additional parameters, DDT and DDI become slightly larger, but not significantly. And the values of ΔZWD became significantly larger. This also indicates that the increase in the number of unknown parameters leads to a weaker structure of the observed equations, which in turn leads to a worse precision of the estimated unknown parameters. In addition, in the three newly added parameters, the errors in the north and east directions are smaller than in the up direction.

3.3 *Comparison of using and not using regularization methods*

As demonstrated in the preceding section, the introduction of three additional unknown parameters has diminished the robustness of the observational equations, consequently leading to a decrease in the precision of the solutions. To counteract this, we have implemented regularization techniques to improve accuracy. To evaluate the impact of the regularization method on enhancing the precision of experimental outcomes, we have used the same data as in the previous section, choosing the results of the baselines established by the HKPC and HKST stations as a case study. The time series of regularization parameter α of baseline HKST-HKPC over time is showed in Fig. 4, and the time series of the solutions for the three baselines are depicted in Fig. 6. A too small α will not fully utilize the contribution of the observations, while a α that is too large will lead to over-regularization, making the solution more biased. The regularization parameter computed by the mean square error minimization criterion that we adopt maximizes the utilization of the contribution of the solution. From the results in Fig. 5, the regularization parameter itself varies significantly between epochs, which is related to the variation of observation conditions. It is important to note that the regularization parameter is very sensitive to observational condition and quality of the data. The results shown in Figure 4 are not universally applicable, we recommend that users calculate customized regularization parameters using their own data based on the methodology outlined in this study.

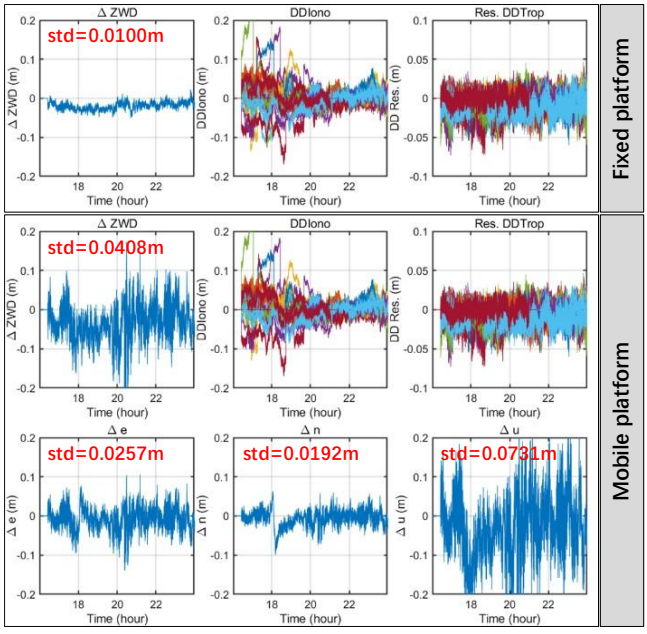

Figure 3. Time series of tropospheric delays (ΔZWD), relative coordinates (Δe, Δn and Δu), and double-difference atmospheres (DDI and DDT) with and without estimation of relative coordinates for baseline HKST-HKPC (smaller is better).

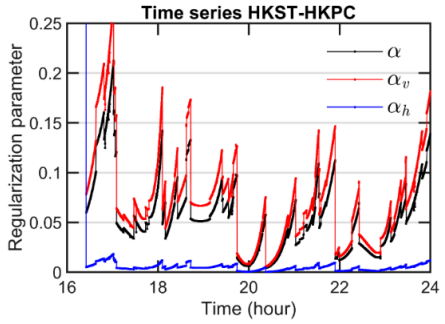

Figure 4. Regularization parameter α of baseline HKST-HKPC over time.

We show the results without regularization in the up panels of Fig. 5 (labelled "Without regularization"), and with regularization in the bottom panels (labelled "With regularization"). The standard deviation of the time series is also given in the figures. From the results shown in the figures, it is evident that the DDIono and DDTrop residues exhibit no significant changes after applying the regularization method. Further analysis confirms that only a slight reduction in the number of valid observations occurs. In addition, the accuracies of the tropospheric delay and the relative movement of the base station are significantly improved, especially when the tropospheric delay ΔZWD, and the movement in the up direction Δu, are significantly reduced. In addition, Δe and Δn also become significantly smaller, but the magnitude of the change is smaller than that in the up direction. This suggests that the regularization method is mainly used for the decorrelation of coordinates in the tropospheric delay and up directions, but is also effective in improving the accuracy of coordinates in the north and east directions.

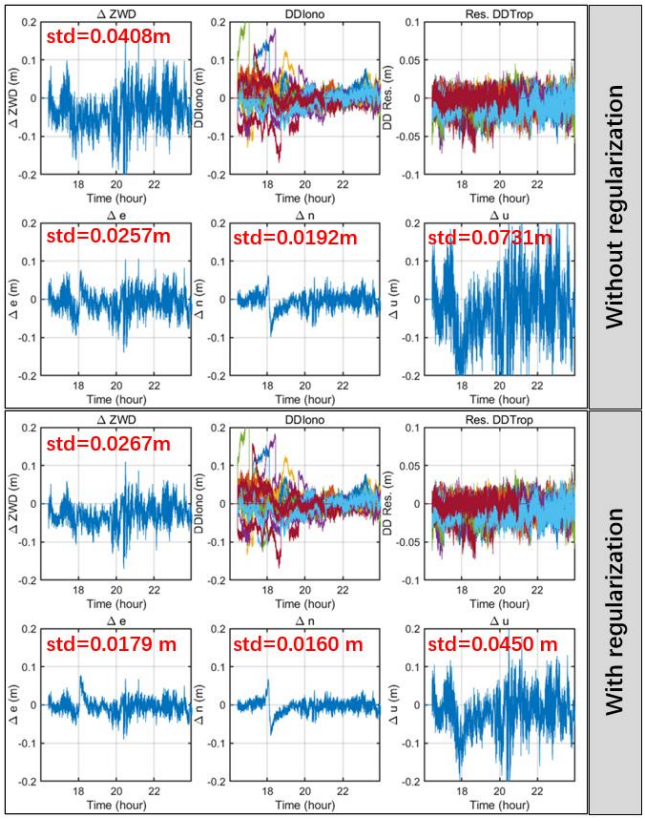

Figure 5. Time series of tropospheric delays (ΔZWD), relative coordinates (Δe, Δn and Δu), and double-difference atmospheres (DDI and DDT) with general method and regularization method for baseline HKST-HKPC (STD smaller is better).

Table 3 presents a comparison of the baseline results with and without the regularization method. The number of baselines in the table is greater than that shown in Fig. 2. This is because the Delaunay triangulation network is constructed in real-time. Some epochs have missing data, which leads to the update of the baselines. The table is arranged in descending order of baseline length from top to bottom. We have marked in red in the table the results with values larger than 5 cm. It can be observed that the vast majority of the STDs of ΔZWD and Δu are larger than 5 cm without using the regularization method, and nearly half of the Δe and Δn are larger than 5 cm. However, after using the regularization method, almost all the results are smaller than 5 cm, and most of them are smaller than 5 cm. This indicates that the errors in the upward direction and tropospheric delays are most correlated, and the regularization method is mainly used to decorrelate them. Of course, the regularization method also contributes to improving the accuracy of the north and east-oriented coordinates, but the contribution in this regard is weaker than the former.

Table 3. Comparison of using and not using regularization methods

Baseline	Length	STD of general method (cm)				STD of regularization method (cm)			
	(km)	ΔZWD	Δe	Δn	Δu	ΔZWD	Δe	Δn	Δu
HKTK-HKLT	27.3	6.02	7.98	4.29	6.01	3.13	2.35	2.09	3.11
HKNP-HKLM	23.5	2.98	1.30	0.94	3.23	2.29	1.23	0.81	2.65
HKOH-HKWS	23.5	3.77	2.07	1.40	5.08	2.34	1.70	1.14	3.63
HKST-HKLM	20.7	4.51	3.23	1.85	4.98	2.70	1.33	1.25	2.37
HKST-HKPC	19.4	5.17	11.06	3.04	5.76	6.23	2.67	2.73	2.79
HKKT-HKPC	18.0	5.48	2.23	1.41	5.56	2.60	1.58	1.35	3.29
HKWS-HKTK	17.0	6.44	4.62	4.15	5.94	3.14	2.43	1.68	3.47
HKLT-T430	16.9	3.05	1.76	1.16	4.72	2.30	1.35	1.03	3.47
HKPC-HKLT	15.4	4.61	1.93	1.13	5.27	2.18	1.33	1.15	2.88
T430-HKSS	15.2	5.54	4.91	2.47	5.50	2.34	2.29	1.21	4.45
HKSL-HKNP	14.1	3.44	2.10	1.21	4.87	1.93	1.35	0.80	2.96
HKPC-HKCL	13.4	4.57	6.09	3.50	4.56	6.51	2.24	1.34	3.27
HKLM-HKMW	12.7	3.62	1.93	1.39	4.49	3.07	1.38	1.01	3.08
HKLM-HKOH	11.6	4.82	2.04	2.59	3.89	2.17	1.42	1.01	2.57
HKNP-HKMW	11.3	3.01	2.03	1.14	4.34	2.17	1.32	0.98	3.19
HKMW-HKCL	10.8	4.34	6.32	3.96	5.03	2.52	1.45	1.00	2.90
HKSS-HKST	9.6	5.01	3.53	2.07	5.29	2.93	2.15	1.38	4.10
HKKT-T430	9.2	4.84	4.70	3.02	5.37	1.90	1.39	0.94	3.32
HKCL-HKSL	8.7	5.65	4.74	4.31	6.00	3.01	1.40	1.09	2.73
HKLT-HKSL	8.7	3.36	6.29	3.69	4.43	5.57	1.19	0.97	2.55
HKLT-HKKT	7.8	5.65	2.24	4.06	5.47	1.89	1.36	0.96	2.90
HKWS-HKSS	6.8	4.84	2.41	1.50	5.19	2.93	2.15	1.18	3.99
HKNP-HKCL	5.4	2.94	3.41	1.61	3.77	2.96	1.54	1.17	2.74
HKMW-HKPC	4.8	3.68	2.59	1.90	5.01	2.54	1.40	1.04	3.44

*The red are values greater than 5.00 cm.

Figure 6 presents the solution results for 24 baselines, illustrating the standard deviations (STDs) of Δe, Δn, Δu, and ΔZWD both with and without the regularization method. The baselines are ordered from left to right in reverse order of their lengths, with the longest baseline, HKTK-HKLT, at 27.3 km on the far left, and the shortest baseline, HKMW-HKPC, at 4.8 km on the far right. The figure demonstrates that the regularization method significantly enhances the accuracy of the unknown parameters, particularly ΔZWD and Δu. There is no significant correlation between this accuracy improvement and the baseline length. However, it is observed that the regularization method may reduce the accuracy of Δe and Δn for baselines longer than 15 km (left side of baseline HKSL-HKPC).

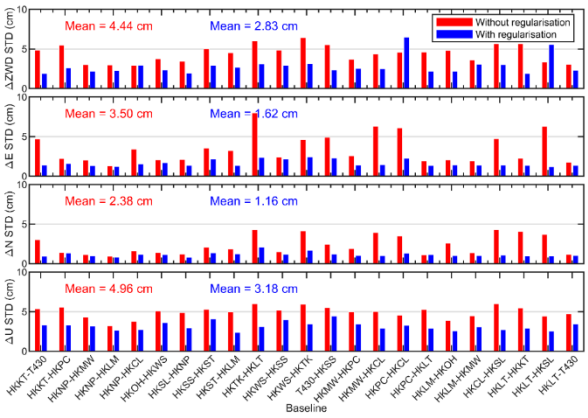

Figure 6. Comparison of STDs in the ΔE, ΔN, and ΔU directions of coordinates and ΔZWD using the regularization method and without applying the regularization method.

3.4 *Verification of positioning results*

The comparison of the baseline parameter estimation results has demonstrated the effectiveness of the algorithm. To further validate the proposed method, we perform positioning validation from the user side. We convert fixed station observations into mobile station observations by adding periodic noise. The generation of periodic noise is as follows:

$$\begin{aligned}\Delta e &= A_1 \sin\left(B_1 t + C_1\right) + A_2 \sin\left(B_2 t + C_2\right)\\ \Delta n &= A_3 \sin\left(B_3 t + C_3\right) + A_4 \cos\left(B_4 t + C_4\right)\\ \Delta u &= A_5 \cos\left(B_5 t + C_5\right) + A_6 \cos\left(B_6 t + C_6\right)\end{aligned} \tag{28}$$

where A, B and C are parameters of the periodic function, which have different values at different stations to simulate the different movements of different sites. After generating the periodic noise, it is projected to each satellite direction and then added to the pseudo-range and phase observations of the fixed station (as the followed equations), after which the station is converted to a mobile station.

$$\begin{aligned}&[\Delta x, \Delta y, \Delta z] = enu2xyz([\Delta e, \Delta n, \Delta u])\\ &P_{r\ mobile}^{s} = P_{r\ fixed}^{s} + mf_r^s([\Delta x, \Delta y, \Delta z])\\ &\Phi_{r\ mobile}^{s} = \Phi_{r\ fixed}^{s} + mf_r^s([\Delta x, \Delta y, \Delta z])\end{aligned} \tag{29}$$

where *enu2xyz* is the coordinate conversion function, $P_{r\ mobile}^{s}$ and $\Phi_{r\ mobile}^{s}$ are pseudorange and carrier phase from satellite r to receiver s, the mf_r^s is the mapping function from the coordinates to line of sight of the signals.

To verify the effectiveness of this simulated mobile station, we used precise point positioning (PPP) and real-time kinematic (RTK) to conduct positioning experiments on the user station. The RTK experiment is divided into two sub-solutions: fixed base and mobile base according to the different base stations used as references. In addition, we also conducted NRTK positioning experiments, which are also divided into fixed and mobile solutions according to different base stations. In the mobile solution, there are two sub-solutions according to whether the baseline of server side uses regularization method. These experimental settings are summarized in Table 4, and are named solutions S1–S6, respectively.

Table 4. Experiment setting of six solutions

Solution	Base	Rover	Method	Regularization
S1	---	mobile	PPP	---
S2	fixed	mobile	RTK	---
S3	mobile	mobile	RTK	---
S4	fixed	mobile	NRTK	---
S5	mobile	mobile	NRTK	Without regularization
S6	mobile	mobile	NRTK	With regularization

Figure 7 shows the PPP result (Solution S1). The points in the left panels of the figure are the error time series with the fixed coordinates as the reference, the line is the periodic noise generated according to Eq. (28), and the right panels of the figure are the time series of the difference between the two, that is, the positioning error with the position of the mobile coordinates as the reference. From the left panel, it can be noticed that the horizontal positioning result of PPP is very consistent with the noise added to the observation value, and the U direction is slightly worse. The positioning errors in the three directions of E, N, U, are 0.74 cm, 0.43 cm, 1.74 cm.

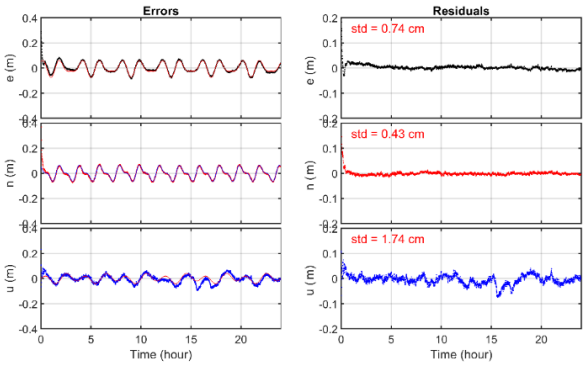

Figure 7. Precise point Positioning (PPP) results (Solution S1) of the mobile user station (with periodic movements). The left panels are the error time series with reference to the fixed station coordinates (i.e., points, the lines are periodic motions), and the right panels are the residual series with reference to the coordinates after periodic motion. The upper, middle, and lower panels are the E, N, and U directions, respectively.

Figure 8 shows the RTK result (Solution S2), the points and lines in this figure have the same meaning as Figure 8. From the results, the RTK positioning results are worse than those of PPP, because only float solutions can be obtained in some epochs (marked with gray background). The errors in the three directions of E, N, U are 1.92 cm, 2.79 cm, 4.21 cm, the fixing rate is 97.74%.

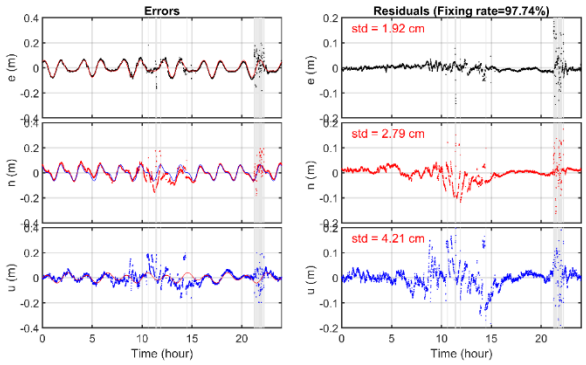

Figure 8. Real-time kinematic (RTK) results (Solution 2) of the mobile user station with periodic movements, with fixed base station. The rest is the same as Figure 7.

Figure 9 is the same as Figure 8, except that the base station is replaced by a mobile station (Solution S3). In other words, it is the RTK positioning result of all stations that are mobile. The waveform in the figure is different from the previous one because the movement of the base station is also transmitted to the positioning result along with the observation value. It can be found that the RTK positioning results in all three directions when all the stations are mobile, and the fixing rate also drops to 88.06%.

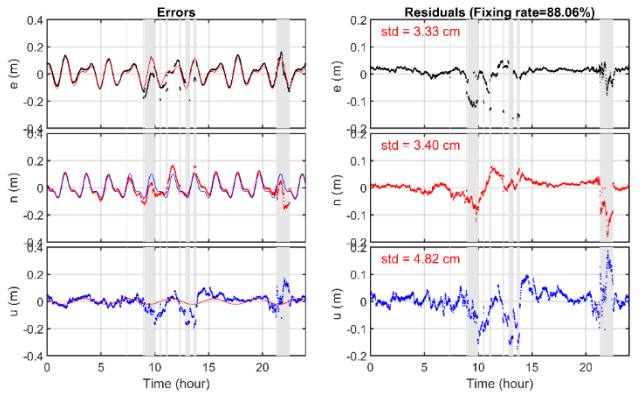

Figure 9. Real-time kinematic (RTK) results (Solution S3) of the mobile user station with periodic movements, with mobile base station. The rest is the same as Figure 7.

Figure 10 shows the positioning result of NRTK with the fixed base station, which is the general NRTK (Solution S4). It can be found that the result is less accurate than Solution S3, but the fixing rate is higher, but still lower than Solution S2.

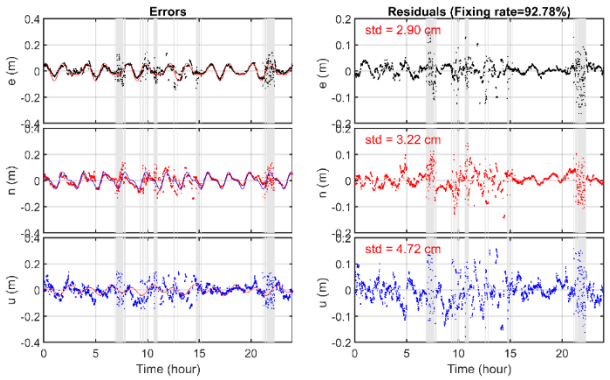

Figure 10. Network real-time kinematic (NRTK) results (Solution S4) of the mobile user station with periodic movements, with fixed network base station. The rest is the same as Figure 7.

Figure 11 and Figure 12 are the NRTK positioning results of the user side when the server does not use the regularization method and when it uses the regularization method (Solution S5 and S6). Both figures are the results of the base station and the user station being the mobile station. There is no significant difference between the two results, which is predictable, because the regularization method is mainly used by the server-side baseline solution to decorrelate the baseline movement and the atmosphere, and the atmosphere itself is not sensitive to small movements during the interpolation process. However, the positioning result is still within the normal accuracy that RTK can achieve, that is, 2-3 cm horizontally and about 5 cm in vertical direction, which can prove the effectiveness of this new method.

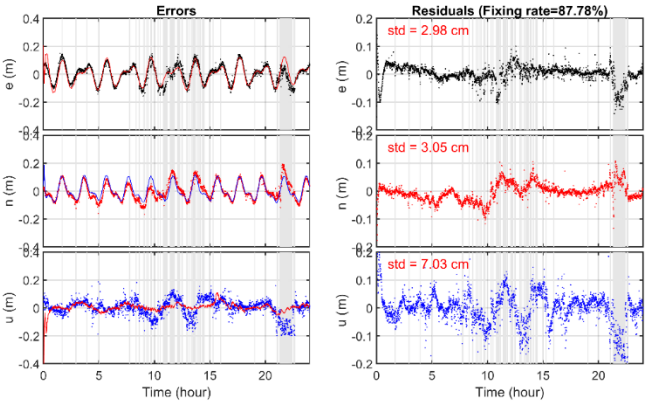

Figure 11. Network real-time kinematic (NRTK) results (Solution S5) of the mobile user station with periodic movements, with mobile network base station and without regularization. The rest is the same as Figure 7.

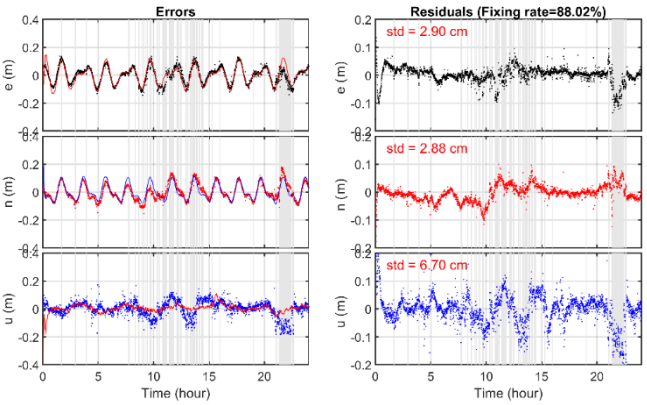

Figure 12. Network real-time kinematic (NRTK) results (Solution S6) of the mobile user station with periodic movements, with mobile network base station and with regularization. The rest is the same as Figure 7.

We show the result statistics of the 6 solutions in Table 5, i.e., the accuracy and fixing rate in the three directions of E, N, and U. Experimental analysis reveals that moving the fixed reference stations induces measurable degradation in positioning accuracy and ambiguity resolution rates. However, the resultant precision (remaining within practical operational tolerances) validates the methodological framework proposed for oceanic NRTK implementation. This finding confirms the technical feasibility of extending NRTK capabilities to marine environments through adaptive station deployment strategies.

Table 5. Positioning results and fixing rate of six solutions

Solution	E (cm)	N (cm)	U (cm)	Fixing rate (%)	Convergence time
S1	0.74	0.43	1.74	---	~ 30 min
S2	1.92	2.79	4.21	97.74	Seconds
S3	3.33	3.40	4.82	88.06	Seconds
S4	2.90	3.22	4.32	92.78	Seconds
S5	2.98	3.05	7.03	87.78	Initialization: ~30 min Follow-up: seconds
S6	2.90	2.88	6.70	88.02	Initialization: ~30 min Follow-up: seconds

4 CONCLUSIONS

In this contribution, we propose a novel network RTK solution for mobile platforms to extend high-precision

network RTK positioning service to marine areas. In this solution, all base stations are assumed to be anchored to ocean buoys, which are constrained by an anchor chain to move with the waves over a limited range of the sea surface. The proposed method incorporates baseline motions, specifically Δx, Δy, and Δz, into the unknown parameters of the baseline solution, then the regularization method is subsequently employed to mitigate the degradation of the equation structure caused by the introduction of additional unknowns, while also serving to decorrelate these parameters and enhance the accuracy of the solutions for the unknown parameters. Finally, PPP is performed on one or more of the stations to provide an absolute position reference for the network.

Observations from 15 CORS stations in the Hong Kong were utilized to experimentally validate the feasibility of the proposed method. The experimental results indicate that while the introduction of unknown parameters does result in a degradation of tropospheric delay accuracy, it has no significant impact on DD troposphere delay and DD ionospheric delay. Furthermore, the regularization technique proves effective in enhancing the accuracy of these unknown parameters, with the average standard deviations of e, n, u, and ZWD for 24 baselines decreasing from 4.44/3.50/2.38/4.96 cm to 2.83/1.62/1.16/3.18 cm. From the positioning results, although the positioning accuracy of the mobile platform is reduced compared to the fixed platform, it can still reach the centimetre level, which is still at the level of normal NRTK accuracy. In addition, the new NRTK service initially requires a longer convergence time similar to PPP during startup, but subsequently achieves rapid convergence comparable to fixed base NRTK, delivering consistent and stable service thereafter.

This technology can be combined with existing fixed base station NRTK (such as HK CORS) to expand the existing high-precision positioning services on land to offshore areas. Our next step will be to gather data from the offshore marine GNSS buoys to further develop this maritime NRTK system.

ACKNOWLEDGMENTS

The authors would like to thank the Geodetic Survey Section of Survey and Mapping Office of Hong Kong for providing GNSS observation data.

FUNDING

This research is funded by the General Research Fund of Hong Kong (Grant No. 15229622) and the Innovation and Technology Fund of Hong Kong (Grant No. ITP/019/22LP).

DATA AVAILABILITY

The software platform of this paper is Network RTK software "Venus". The GNSS observations data are obtained from the Hong Kong Satellite Positioning Reference Station Network (SatRef): https://www.geodetic.gov.hk/en/satref/satref.htm.

REFERENCES

[1] El-Sheimy, N., Lari, Z. "GNSS Applications in Surveying and Mobile Mapping," in Position, Navigation, and Timing Technologies in the 21st Century: Integrated Satellite Navigation, Sensor Systems, and Civil Applications, vol. 2, pp. 1711–1733, 2020. doi: 10.1002/9781119458555.ch55.

[2] Guo, J., Li, X., Li, Z., Hu, L., Yang, G., Zhao, C., ... Ge, M. "Multi-GNSS precise point positioning for precision agriculture," Precision Agric., vol. 19, pp. 895–911, 2018. doi: 10.1007/s11119-018-9563-8.

[3] Li, X., Guo, B., Lu, C., Ge, M., Wickert, J., Schuh, H. "Real-time GNSS seismology using a single receiver," Geophys. J. Int., vol. 198, no. 1, pp. 72–89, 2014. doi: 10.1093/gji/ggu113.

[4] Joubert, N., Reid, T. G., Noble, F. "Developments in modern GNSS and its impact on autonomous vehicle architectures," in Proc. IEEE Intell. Veh. Symp. (IV), pp. 2029–2036, 2020. doi: 10.1109/IV47402.2020.9304840.

[5] Yu, K., Rizos, C., Burrage, D., Dempster, A. G., Zhang, K., Markgraf, M. "An overview of GNSS remote sensing," EURASIP J. Adv. Signal Process., 2014. doi: 10.1186/1687-6180-2014-134.

[6] Jin, S., Feng, G. P., Gleason, S. "Remote sensing using GNSS signals: Current status and future directions," Adv. Space Res., vol. 47, no. 10, pp. 1645–1653, 2011. doi: 10.1016/j.asr.2011.01.036.

[7] O. Montenbruck et al., "The Multi-GNSS Experiment (MGEX) of the International GNSS Service (IGS)–achievements, prospects and challenges," Adv. Space Res., vol. 59, no. 7, pp. 1671–1697, 2017. doi: 10.1016/j.asr.2017.01.011.

[8] J. Wang, "Stochastic Modeling for Real-Time Kinematic GPS/GLONASS Positioning," Navigation, vol. 46, no. 4, pp. 297–305, 1999. doi: 10.1002/j.2161-4296.1999.tb02416.x.

[9] N. Shen et al., "Short-term landslide displacement detection based on GNSS real-time kinematic positioning," IEEE Trans. Instrum. Meas., vol. 70, pp. 1–14, 2021. doi: 10.1109/TIM.2021.3055278.

[10] C. Kee, B. W. Parkinson, and P. Axelrad, "Wide area differential GPS," Navigation, vol. 38, no. 2, pp. 123–145, 1991. doi: 10.1002/j.2161-4296.1991.tb01720.x.

[11] L. Gauthier et al., "EGNOS: the first step in Europe's contribution to the global navigation satellite system," ESA Bull., no. 105, pp. 35–42, 2001.

[12] X. Chen et al., "Trimble RTX, an innovative new approach for network RTK," in Proc. 24th Int. Tech. Meeting Sat. Div. Inst. Navig. (ION GNSS 2011), pp. 2214–2219, 2011.

[13] P. Steigenberger et al., "Galileo orbit and clock quality of the IGS Multi-GNSS Experiment," Adv. Space Res., vol. 55, no. 1, pp. 269–281, 2015. doi: 10.1016/j.asr.2014.06.030.

[14] F. Yang et al., "Performance evaluation of kinematic BDS/GNSS real-time precise point positioning for maritime positioning," J. Navig., vol. 72, no. 1, pp. 34–52, 2019. doi: 10.1017/S0373463318000644.

[15] P. Enge et al., "Wide area augmentation of the global positioning system," Proc. IEEE, vol. 84, no. 8, pp. 1063–1088, 1996. doi: 10.1109/JPROC.1996.852670.

[16] X. Zhang, X. Li, and F. Guo, "Satellite clock estimation at 1 Hz for realtime kinematic PPP applications," GPS Solut., vol. 15, pp. 315–324, 2011. doi: 10.1007/s10291-010-0191-7.

[17] A. Mart´ın, A. B. Anquela, A. Dimas-Pag´es, and F. Cos-Gay´on, "Validation of performance of real-time kinematic PPP: A possible tool for deformation monitoring," Measurement, vol. 69, pp. 95–108, 2015. doi: 10.1016/j.measurement.2015.03.026.

[18] J. Geng, F. N. Teferle, X. Meng, and A. H. Dodson, "Towards PPP-RTK: Ambiguity resolution in real-time precise point positioning," Adv. Space Res., vol. 47, no. 10, pp. 1664–1673, 2011. doi: 10.1016/j.asr.2010.03.030.

[19] R. M. Alkan, S. Erol, V. ˙Ilc¸i, and ˙I. M. Ozulu, "Comparative analysis of real-time kinematic and PPP

techniques in dynamic environment," Measurement, vol. 163, p. 107995, 2020. doi: 10.1016/j.measurement.2020.107995.
[20] S. Erol, R. M. Alkan, ˙I. M. Ozulu, and V. ˙Ilc¸i, "Performance analysis of real-time and post-mission kinematic precise point positioning in marine environments," Geodesy and Geodynamics, vol. 11, no. 6, pp. 401–410, 2020. doi: 10.1016/j.geog.2020.09.002.
[21] M. El-Diasty and M. Elsobeiey, "Precise Point Positioning Technique with IGS Real-Time Service (RTS) for Maritime Applications," Positioning, vol. 6, pp. 71–80, 2015. doi: 10.4236/pos.2015.64008.
[22] R. M. Alkan, M. H. Saka, ˙I. M. Ozulu, and V. ˙Ilc¸i, "Kinematic precise point positioning using GPS and GLONASS measurements in marine environments," Measurement, vol. 109, pp. 36–43, 2017. doi: 10.1016/j.measurement.2017.05.054.
[23] F. Yang, L. Li, L. Zhao, and C. Cheng, "GPS/BDS Real-Time Precise Point Positioning for Kinematic Maritime Positioning," in Proc. China Sat. Nav. Conf. (CSNC), vol. III, pp. 295–307, Springer Singapore, 2017.
[24] Y. Yang, W. Gao, S. Guo, Y. Mao, and Y. Yang, "Introduction to BeiDou-3 navigation satellite system," Navigation, vol. 66, no. 1, pp. 7–18, 2019. doi: 10.1002/navi.291.
[25] N. Tunalioglu, T. Ocalan, and A. H. Dogan, "Precise point positioning with GNSS raw measurements from an android smartphone in marine environment monitoring," Marine Geodesy, vol. 45, no. 3, pp. 274–294, 2022. doi: 10.1080/01490419.2022.2027831.
[26] Dong, Y., Zhang, L., Wang, D., Li, Q., Wu, J., Wu, M. (2020). Low-latency, high-rate, high-precision relative positioning with moving base in real time. GPS Solut., 24, 1–13. doi: 10.1007/s10291-020-0969-1.
[27] Hou, X., Fang, K., Wang, Z., Li, Q., Fang, J. (2020, January). Research on ambiguity solution integrity monitoring for moving base RTK. In Proceedings of the 2020 International Technical Meeting of The Institute of Navigation (pp. 468–486). doi: 10.33012/2020.17156.
[28] Wang, Z., Hou, X., Dan, Z., Fang, K. (2023). Adaptive Kalman filter based on integer ambiguity validation in moving base RTK. GPS Solut., 27(1), 34. doi: 10.1007/s10291-022-01367-4.
[29] Lygouras, E., Gasteratos, A. (2021). A novel moving-base RTK-GPS-Based wearable apparatus for precise localization of humans in peril. Microprocess. Microsyst., 82, 103833. doi: 10.1016/j.micpro.2021.103833.
[30] Kim, B. G., Kim, D., Song, J., Kee, C. (2024). Expanding Network RTK Coverage Using an Ionospheric-Free Combination and Kriging for Tropospheric Delay. NAVIGATION: J. Inst. Nav., 71(3). doi: 10.33012/navi.662.
[31] A. H. Dodson, W. Chen, N. T. Penna, and H. C. Baker, "GPS estimation of atmospheric water vapour from a moving platform," J. Atmos. Solar-Terrestrial Phys., vol. 63, no. 12, pp. 1331–1341, 2001. doi: 10.1016/S1364-6826(00)00251-0.
[32] T. Ford, M. Hardesty, and M. Bobye, "Helicopter ship board landing system," in Proc. 18th Int. Tech. Meeting Sat. Div. Inst. Navig. (ION GNSS 2005), Long Beach, CA, USA, Sep. 2005, pp. 979–988.
[33] B. Li, Z. Zhang, N. Zang, and S. Wang, "High-precision GNSS ocean positioning with BeiDou short-message communication," J. Geod., vol. 93, pp. 125–139, 2019. doi: 10.1007/s00190-018-1145-z.
[34] J. Geng, F. N. Teferle, X. Meng, and A. H. Dodson, "Kinematic precise point positioning at remote marine platforms," GPS Solut., vol. 14, pp. 343–350, 2010. doi: 10.1007/s10291-009-0157-9.
[35] K. He, D. Weng, S. Ji, Z. Wang, W. Chen, and Y. Lu, "Ocean real-time precise point positioning with the BeiDou short-message service," Remote Sens., vol. 12, no. 24, p. 4167, 2020. doi: 10.3390/rs12244167.
[36] T. Trombetti et al., "On the seafloor horizontal displacement from GPS and compass data in the Campi Flegrei caldera," J. Geod., vol. 97, no. 6, p. 62, 2023. doi: 10.1007/s00190-023-01751-z.
[37] M. Sato et al., "Improvement of GPS/acoustic seafloor positioning precision through controlling the ship's track line," J. Geod., vol. 87, no. 9, pp. 825–842, 2013. doi: 10.1007/s00190-013-0649-9.
[38] S. Xue, Y. Yang, and W. Yang, "Single-differenced models for GNSS-acoustic seafloor point positioning," J. Geod., vol. 96, no. 5, p. 38, 2022. doi: 10.1007/s00190-022-01613-0.
[39] S. Ji et al., "High-precision Ocean navigation with single set of BeiDou short-message device," J. Geod., vol. 93, pp. 1589–1602, 2019. doi: 10.1007/s00190-019-01273-7.
[40] L. C. Tsai et al., "Coastal sea-surface wave measurements using software-based GPS reflectometers in Lanyu, Taiwan," GPS Solut., vol. 25, no. 4, p. 133, 2021. doi: 10.1007/s10291-021-01167-2.
[41] Li, Z., Guo, F., Zhang, X., Guo, Y., Zhang, Z. (2024). Analysis of factors influencing significant wave height retrieval and performance improvement in spaceborne GNSS-R. GPS Solut., 28(2), 64. doi: 10.1007/s10291-023-01605-3.
[42] Li, Z., Guo, F., Zhang, X., Zhang, Z., Zhu, Y., Yang, W., ... Yue, L. (2024). Integrating spaceborne GNSS-R and SMOS for sea surface salinity retrieval using artificial neural network. GPS Solut., 28(4), 1–12. doi: 10.1007/s10291-024-01709-4.
[43] Vergados, P., Krishnamoorthy, S., Martire, L., Mrak, S., Komj´athy, A., Morton, Y. T. J., Vilibi´c, I. (2023). Prospects for meteotsunami detection in earth's atmosphere using GNSS observations. GPS Solut., 27(4), 169. doi: 10.1007/s10291-023-01492-8.
[44] Sch¨one, T., Pandoe, W., Mudita, I., Roemer, S., Illigner, J., Zech, C., Galas, R. (2011). GPS water level measurements for Indonesia's Tsunami Early Warning System. Nat. Hazards Earth Syst. Sci., 11(3), 741–749. doi: 10.5194/nhess-11-741-2011.
[45] Kim, G., Park, W., Park, B. (2024, January). Moving Baseline RTK-based Ground Vehicle-Drone Combination System. In Proceedings of the 2024 International Technical Meeting of The Institute of Navigation (pp. 630–636). doi: 10.33012/2024.19577.
[46] Li, B., Feng, Y., Shen, Y., Wang, C. (2010). Geometry-specified troposphere decorrelation for sub centimeter real-time kinematic solutions over long baselines. J. Geophys. Res. Solid Earth, 115(B11). doi: 10.1029/2010JB007549.
[47] Morozov, V. A. (1984). Methods for solving incorrectly posed problems. Springer Science Business Media. doi: 10.1112/blms/17.6.621.
[48] Golub, G. H., Heath, M., Wahba, G. (1979). Generalized cross-validation as a method for choosing a good ridge parameter. Technometrics, 21(2), 215–223.
[49] Hansen, P. C. (1992). Analysis of discrete ill-posed problems by means of the L-curve. SIAM Rev., 34(4), 561–580. doi: 10.1137/1034115.
[50] Hansen, P. C., O'Leary, D. P. (1993). The use of the L-curve in the regularization of discrete ill-posed problems. SIAM J. Sci. Comput., 14(6), 1487–1503. doi: 10.1137/0914086.
[51] Xu, P. (1998). Mixed Integer Geodetic Observation Models and Integer Programming with Applications to GPS Ambiguity Resolution. J. Geodetic Soc. Jpn., 44(3), 169–187. doi: 10.11366/sokuchi1954.44.169.
[52] Li, B. (2010). Theory and Method of Parameter Estimation for Mixed integer GNSS Stochastic and Function Models. Tongji University, PhD Thesis, pp. 57–58.
[53] Shen, Y., Xu, H. (2002). Spectral decomposition formula of regularization solution for ill-posed equation. J. Geodesy Geodynamics, 22(3), 10–14. doi: 10.14075/j.jgg.2002.03.004.